remote sensing

MDPI

Article

Contactless X-Band Detection of Steel Bars in Cement: A Preliminary Numerical and Experimental Analysis

Adriana Brancaccio † **and Simone Palladino** †,*

Engineering Department, University of Campania "L. Vanvitelli", Via Roma, 29, 81031 Aversa, Italy; adriana.brancaccio@unicampania.it

* Correspondence: simone.palladino@unicampania.it; Tel.: +39-081-5010270

† These authors contributed equally to this work.

Abstract: This work presents preliminary experimental results for advancing non-destructive testing methods for detecting steel bars in cement via contactless investigations in the X-band spectrum. This study reveals the field's penetration into cement, extracting insights into embedded bars through scattered data. Applying a quasi-quadratic inverse scattering technique to numerically simulated data yields promising results, confirming the effectiveness and reliability of the proposed approach. In this realm, using a higher frequency allows for the use of lighter equipment and smaller antennas. Identified areas for improvement include accounting for antenna behavior and establishing the undeformed target morphology and precise orientation. Transitioning from powder-based and sand specimens to real, solid, reinforced concrete structures is expected to alleviate laboratory challenges. Although accurately determining concrete properties such as its relative permittivity and conductivity is essential, it remains beyond the scope of this study. Finally, overcoming these challenges could significantly enhance non-invasive testing, improving structural health monitoring and disaster prevention.

Keywords: contactless GPR; X-band measurements; steel bars detection; cement; microwave imaging

Citation: Brancaccio, A.; Palladino, S. Contactless X-Band Detection of Steel Bars in Cement: A Preliminary Numerical and Experimental Analysis. *Remote Sens.* **2024**, *16*, 2037. https://doi.org/10.3390/rs16112037

Academic Editor: Fabio Tosti

Received: 29 March 2024
Revised: 31 May 2024
Accepted: 4 June 2024
Published: 6 June 2024

1. Introduction

Reinforced concrete represents the predominant technology in the modern built environment, providing essential infrastructure for residential, commercial, and industrial purposes. These structures' durability and structural integrity are crucial for guaranteeing long-term safety and functionality. The necessity of non-invasive procedures for the existing heritage has resulted in the emergence of several non-destructive testing (NDT) methods as indispensable tools in assessing and monitoring reinforced concrete structures. In recent years, there has been a surge in research and development aimed at advancing NDT techniques for reinforced concrete assessment. This surge is driven by the growing need for accurate and reliable evaluation methods to ensure the longevity and performance of existing structures and optimize the design and construction of new ones. Furthermore, given that the plans for many buildings from the latter decades of the previous century are no longer available, there is a strong interest in recovering structural information about these buildings to ensure compliance with current safety standards, including seismic regulations.

The evolution of NDT techniques has been marked by a continual refinement of traditional methods and the emergence of cutting-edge technologies. Modern instrumentation and signal processing algorithms have enhanced traditional methods, such as ultrasonic testing (UT), rebound hammer (RH), and electromagnetic methods, enabling more precise and detailed assessments. Simultaneously, novel approaches, including ground-penetrating radar (GPR), digital image correlation (DIC), and acoustic emission testing (AET), have gained prominence for their ability to provide deeper insights into the internal health of reinforced concrete.

Bensaber et al. (2023) investigated the influence of load on cubic concrete specimens on the accuracy of ultrasonic tests [1]. Yin et al. (2023) proposed a nonlinear ultrasonic technique for in situ monitoring of the cracks and defects of ultra-high-performance fiber-reinforced concrete structures under tensile loads [2]. Kuchipudi and Ghosh (2024) suggested an enhanced method for detecting defects in reinforced concrete using an automated two-stage convolutional neural network [3]. Therefore, Alavi et al. (2024) investigated reinforced concrete specimens' strength by using the SonReb method combined with a machine learning algorithm [4]. However, several other non-destructive tests can investigate the health of reinforced concrete structures. For instance, Jena et al. (2024) investigated a coal mine overburden's effect on strength as a substitute candidate to replace sand in reinforced concrete and analyzed the mechanical response by conducting Schmidt tests [5]. Parhi and Patro (2024) assessed the fracture toughness of reinforced concrete structures by performing a Schmidt test and retrieving the rebound number [6]. Thermal imaging (TI) is efficient for large-scale assessments as a versatile tool in non-destructive tests. In this realm, Keo et al. (2023) and Woldeamanuel et al. (2023) used a thermal imaging tool to investigate the health and strength of existing reinforced concrete structures. Notably, the former applied microwave infrared thermography to detect and characterize defects [7], while the latter proposed a combination of thermal imaging and deep learning techniques for estimating the real strength of reinforced concrete structures [8]. Another insightful tool to investigate the strains of reinforced concrete structures is digital image correlation (DIC). It is an optical method capable of analyzing complex crack patterns, as shown in the works of Cheng et al. (2023) [9], Herbers et al. (2023) [10], and Jin et al. (2023) [11], and through other numerical methods presented by Palladino et al. (2022) [12], Esposito et al. (2024) [13], and Zona et al. (2024) [14].

Several other authors have investigated damage evolution and fracture propagation, such as Sagar and Basu (2023) [15] and Ma et al. (2023) [16], by employing an acoustic emission test (AET), which can detect defects in reinforced concrete by releasing transient stress waves. The combination of different approaches and tests, both numerical and experimental, is beneficial.

The present work delves into another set of tests, namely radar-based ones. Studies on the electromagnetic response of cement date back to the early 1990s, as reported by Robert (1998) [17] and the references therein. In this context, several contact and contactless radar-type tests have emerged and been employed in recent decades due to their capability to work at high frequencies and to penetrate deeply into the concrete. For instance, Barrile and Pucinotti (2005) proposed applying contact-type georadar technology on civil buildings [18]. Pasculli et al. (2018) used a dual-polarized ground-penetrating radar (GPR) to investigate the health status of reinforced concrete bridges [19]. Rhee et al. (2019) proposed an air-coupled GPR to assess the deterioration in concrete bridge decks [20]. Tosti and Ferrante (2020) provided an overview of the literature on GPR techniques and proposed a new methodological approach for assessing reinforced concrete structures [21]. In Chang et al.'s work (2009), several samples of concrete with bars of different diameters and different cover depths are realized and investigated by using a pulsed MALA GPR system (frequency: 1 GHz) combined with a digital imaging correlation technique. In [22], an automated rebar picking algorithm for GPR data of concrete bridge decks is presented. This method is intuitive and useful because the image interpretation is independent from the user's expertise. Finally, Marchisotti and Zappa (2022) studied the possibility of monitoring defects in concrete media by employing a combination of optical time-of-flight sensors (ToF) and drone apparatus [23].

It has to be noted that contactless radar-type tests gained popularity in practical applications only a few years ago because of the modern technological enhancements in lightweight, practical, ready-to-use georadars. However, several difficulties may arise during contactless radar applications due to the distance from structural targets, as reported by Catapano et al. (2021) [24]; the choice of proper operative frequencies to penetrate con-

crete materials; and the limitations in returning accurate measures of reinforced steel bars. Boldrin et al.'s (2024) review on GPR applications refers to frequencies up to 3 GHz [25].

From these perspectives, the present work presents the first experimental attempt to properly evaluate the position of steel bars in cement using the quasi-quadratic inverse scattering algorithm (QQIS) proposed by Brancaccio (2022) [26] using frequencies around 10 GHz, hence providing answers for future real applications in air–drone radar.

2. Mathematical Formulation

Non-destructive evaluation by means of measurements of the electromagnetic field collected "outside" the structure falls among the class of inverse scattering problems: the structure is illuminated by an external electromagnetic source and the field scattered under such illumination depends on the internal status of the structure itself. Once a suitable mathematical relationship is established between the parameters of interest and the scattered field, which is known by means of measurements, inverting such a relationship allows us to recover the parameters' values. This is, as is well known, a nonlinear and ill-posed problem. A complete theoretical insight is beyond the scope of this work; however, it is worth recalling some important features of the interaction between electromagnetic waves and dielectric materials (such as the cement). First, the illuminating field must penetrate and propagate in the structure; otherwise, information about the inside cannot be collected from the outside. So, an evaluation of the power transmitted at the interface and of the attenuation due to internal losses is required. Such a problem is addressed in the following with reference to plane wave propagation.

2.1. Attenuation

It is well known that losses cause the exponential decay of the wave amplitude in the propagation direction. Such a decay can be calculated for a plane wave by looking at the imaginary part of the wavenumber, whose expression is

$$k = \omega\sqrt{\varepsilon_0\mu_0\left(\varepsilon_r - i\frac{\sigma}{\omega\varepsilon_0}\right)} = \beta - i\alpha \tag{1}$$

where $\omega = 2\pi f$ is the angular frequency, $\varepsilon_0 = 8.85 \times 10^{-12}$ F/m is the dielectric permittivity of vacuum, ε_r is the relative permittivity, a vacuum permeability of $\mu_0 = 4\pi \times 10^{-7}$ H/m is assumed, and σ is the material's conductivity, denoting the presence of induced currents. The expression of a wave propagating, for instance, in the direction of the z-axis of a reference system:

$$\mathbf{E}_0 e^{-ikz} = \mathbf{E}_0 e^{-i\beta z} e^{-\alpha z} \tag{2}$$

makes the above-mentioned exponential decay evident, where the imaginary part of k, namely α, provides the attenuation rate per unit length. The reciprocal of α is known as the "propagation depth" because it provides the order of magnitude of the depth above which the wave amplitude becomes negligible.

In Figure 1, α, expressed in dB/dm, is reported as a function of the frequency and of the conductivity for a few different relative permittivity values. It is very interesting to note that above few hundreds of MHz, the frequency value does not significantly affect the attenuation. What seriously negatively effects its ability to penetrate the structure for more than a few centimeters is the conductivity. However, when the relative permittivity increases, the situation becomes more favorable and, notably, higher conductivity values correspond to higher relative permittivity values. We can conclude that the frequency can be much higher than 10 GHz, which still guarantees a penetration of a few decimetres. This result is interesting, because in GPR applications, it is usually assumed that frequencies higher than 1–2 GHz cannot significantly penetrate the investigated material [27].

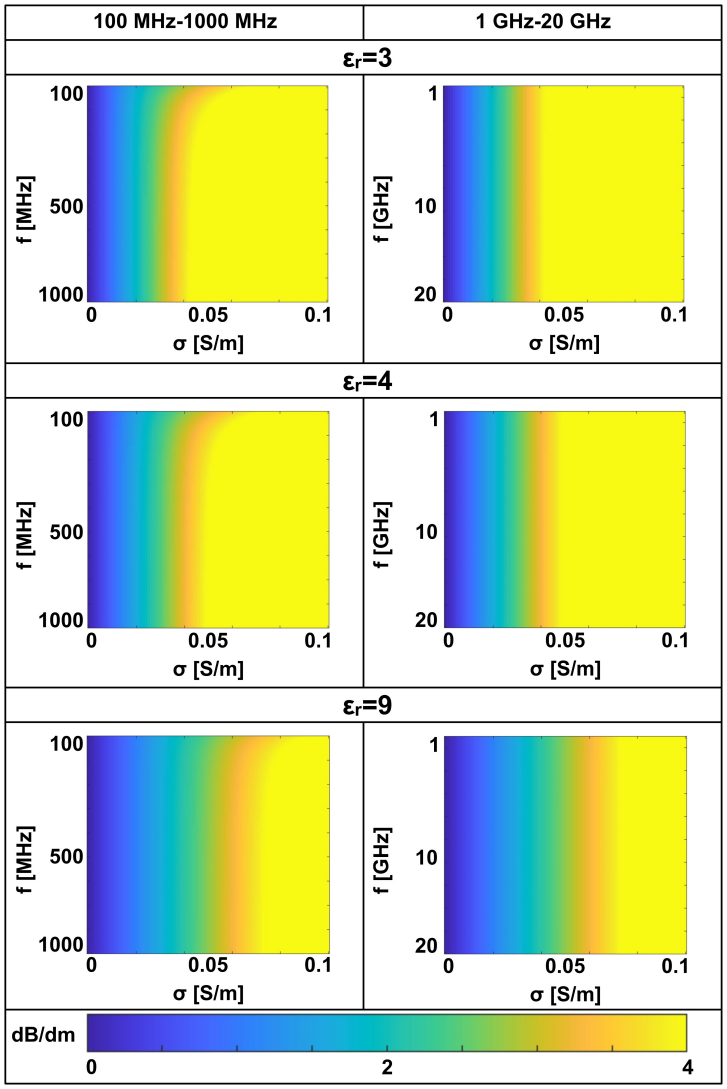

Figure 1. Attenuation in dB/dm vs. frequency and conductivity for different ε_r. Left column $f \in$ [100–1000] MHz; right column $f \in$ [1–20] GHz. Top row $\varepsilon_r = 3$; middle row $\varepsilon_r = 4$; bottom row $\varepsilon_r = 9$.

2.2. Reflection and Transmission

In order to provide a synthetic index, we consider a canonical geometry where a plane wave impinges on the planar interface between air and the dielectric; the letter is denoted by its relative dielectric permittivity ε_r, and $\sigma = 0$ is assumed for brevity. The Fresnel reflection coefficients, for both transverse electric (TE) and transverse magnetic (TM) polarization, provide a way to evaluate how much of the impinging power is reflected and how much is transmitted inside the medium. As is well known, the Fresnel coefficients depend on the incidence angle θ, whereas a dependence on the frequency arises only if the dielectric presents losses, i.e., if ε is complex-valued, which also accounts for the electric conductivity. Assuming again that the relative magnetic permeability is unitary everywhere, the Fresnel coefficients can be written as

$$R_{TE} = \frac{\cos\theta - \sqrt{\varepsilon_r - (\sin\theta)^2}}{\cos\theta + \sqrt{\varepsilon_r - (\sin\theta)^2}}$$
$$R_{TM} = \frac{\sqrt{\varepsilon_r - (\sin\theta)^2} - \varepsilon_r \cos\theta}{\sqrt{\varepsilon_r - (\sin\theta)^2} + \varepsilon_r \cos\theta} \quad (3)$$

In the following, reference is made to the power density carried by each plane wave (incident, transmitted, reflected), i.e., to the power per unit of surface area perpedicular to the direction of wave propagation, provided by the amplitude of the real part of the Poynting vector. The transmitted active power density P_t can be calculated as

$$P_t = P_i(1 - \|R_p\|^2)\frac{\sqrt{\varepsilon_r}\cos\theta}{\sqrt{\varepsilon_r - (\sin\theta)^2}} \tag{4}$$

with $p = TE, TM$, where P_i stands for the incident power density. In Figure 2, the normalized transmitted power, calculated by Equation (4), is shown as a function of the incidence angle for two permittivity values. As it can be appreciated, TM polarization performs better than TE in both cases, providing a higher transmitted power. This is due to the well-known Brewster angle phenomenon. For both polarizations, the transmitted power decreases as the incidence angle θ increases. This reduces the angle of view useful to "illuminate" the structure under test, and must be taken into account in the design of the measurement configuration. In order to better understand the role of the incidence angle, the transmitted power normalized to its maximum value, arising at angle $\theta = 0$, is shown on the right.

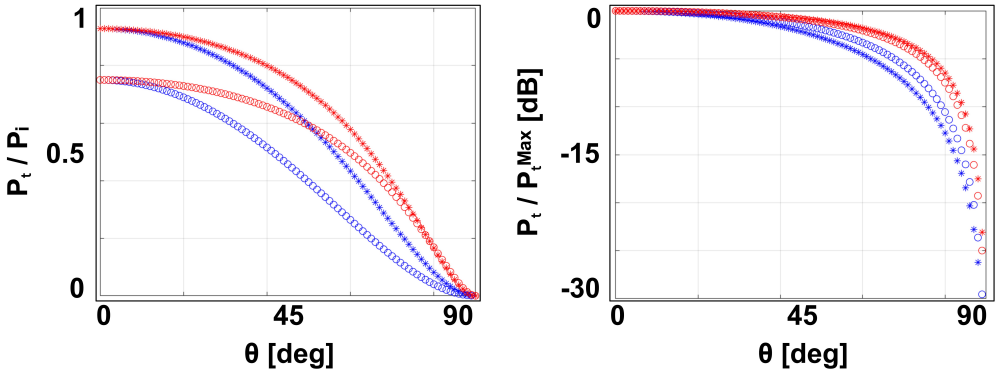

Figure 2. Transmitted power density: TE (blue), TM (red); $\varepsilon_r = 3$ (stars), $\varepsilon_r = 9$ (circles).

The curves in Figure 2 suggest that, in the case of contactless testing at some distance from the target, the angle of view should be kept approximately below 40°.

2.3. Bar Detection and Localization

In order to show the feasibility of NDT of reinforced concrete by contactless measurements at frequencies up to 10 GHz, experimental and simulated data in the X-band (8.2–12.4 GHz) were processed by using the algorithm proposed in [26]. Let us briefly recall the main features of the algorithm. A 2D geometry is assumed. The structure is schematized as a rectangle of width W and depth P, where N_b positions, namely $\mathbf{r}_n, n = 1, ..., N_b$, are "candidates" for the bars. The cement permittivity and the bars' radii are known. The source is a filamentary current placed at $\mathbf{r}_s$. In these hypotheses, the scattered field can be approximated as follows:

$$E(f, \mathbf{r}_s, \mathbf{r}_o) = \sum_{n=1}^{N_b} C_n(k) H_0^{(2)}\left(\frac{2\pi f}{c_o}|\mathbf{r}_s - \mathbf{r}_n|\right) H_0^{(2)}\left(\frac{2\pi f}{c_o}|\mathbf{r}_o - \mathbf{r}_n|\right)\gamma(n) \tag{5}$$

where $\mathbf{r}_o$ is the measurement point, f is the frequency, c_0 is the wave velocity in free space, $H_0^{(2)}(\cdot)$ is the Hankel function of order zero and second kind, the coefficients $C_n(k)$ (whose expression is reported in [26]) depend on the dielectric permittivity and shape (rectangular in the considered case) but not on the measurement point and source positions, and

$$\gamma(n) = \begin{cases} 1 & \text{if there is a bar in } \mathbf{r}_n \\ 0 & \text{if there is } \textit{not} \text{ a bar in } \mathbf{r}_n \end{cases} \tag{6}$$

The model in Equation (5) establishes a linear relationship between the scattered field measured outside the structure under test and the function γ, which represents the problem's unknown quantity. In [26], multimonostatic illumination along a segment from only one side of the structure under test was considered. Here, we consider measurements on a circle all around the structure in a multi-bistatic configuration, where the source and observation points scan the circles $\mathbf{r}_s = (R_s \cos\theta, R_s \sin\theta)$ and $\mathbf{r}_o = (R_o \cos(\theta + \theta_0), R_o \sin(\theta + \theta_0))$, respectively. In Figure 3, the measurement geometry and an example of "candidate" positions among which the bars are searched for are depicted. The inversion of the linear operator (5) is performed via truncated singular value decomposition (TSVD).

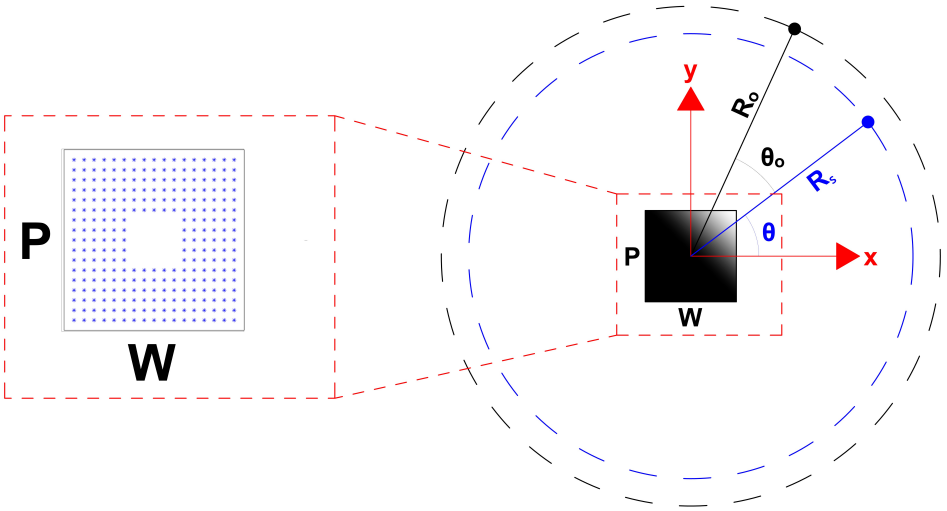

Figure 3. Two-dimensional measurement configuration: the source and the observation points scan the circles of radius R_s and R_o, respectively, at a fixed stand-off angle θ_0. The investigated domain is the rectangle $W \times P$. On the left square zoomed-in section, blue circles represent the unknown bar positions.

3. Experimental Setup

The laboratory experimental test was conducted in a controlled semi-anechoic environment with panels, which guarantees a reflection coefficient at normal incidence of 40 dB at 8 GHz. The measurement setup consists of two horn antennas in the X-band (8.2–12.4 GHz), one transmitting and one receiving, placed at some distance from the target (i.e., the sample to be investigated). The transmitting and receiving antennas are connected by coaxial cables to a Vector Network Analyzer (VNA), model "KEYSIGHT P9373A, 300 kHz–14 GHz" (© Keysight Technologies, Santa Rosa, CA, USA). The operational frequency range represents an innovation in the field of georadar measurements for structural identification. The novelty lies in the fact that standard georadar measurements are typically conducted at frequencies below 1–2 GHz. In order to perform measurements all around the target, the antennas are placed in a fixed position and the target rotates. In this scope, the measurement setup includes a rotating table with a diameter of 250 mm, moved by means of a stepper motor controlled by a Compumotor S-Drive (© Compumotor Division of Parker Hannifin Corporation, Cleveland, OH, USA, 1997). The laboratory experiment was conducted on several square specimens with dimensions of 90 × 90 mm^2 and a height of 450 mm. Some specimens contained only natural dried sand, while others included sand with the presence of steel bars, and some were composed of pozzolanic cement powder (CEM IV/B (P) 32.5 R) with compressive strengths at 2 and 28 days of 10 MPa and 32.5 MPa, respectively, as well as pozzolanic cement powder and steel bars.

The reason for using powder (sand and cement) for this preliminary work is that such a choice allows us to change the bar number and position inside the specimens in quite a simple way.

The steel bars' diameter is 8 mm and their length is 1000 mm. The specimens were placed at the center of the rotating plate, affixed with an ad hoc 3D designed support basement with a circular plan on two levels. The lower level has a diameter of 195 mm, and the upper level has a diameter of 250 mm. This tapered volume solution was conceived to ensure unrestricted rotation of the specimen relative to the footprint of the electromechanical engine. To ensure the vertical positioning of the steel bars within the box-shaped specimen, two square supports of 90×90 mm^2 were created featuring circular voids with a diameter of 9 mm. The geometric models were designed in a CAD environment and transferred to a Bambu Lab X1 Carbon 3D printer (© Bambu Lab, Shenzhen, China) with a maximum build volume of $256 \times 256 \times 256$ mm^3, operating at a maximum hot-end temperature of 300 °C. The filament used for printing was polylactic acid (Bambu Lab PLA Basic) with a density of $\rho = 1.24$ g/cm^3, a tensile strength of $\sigma_t = 35 \pm 4$ MPa, a flexural strength of $\sigma_b = 76 \pm 5$ MPa, and an elastic modulus of $E = 2.7 \pm 0.16 \times 10^3$ MPa. For clarity and comprehensive information, the entire experimental setup is illustrated in Figure 4.

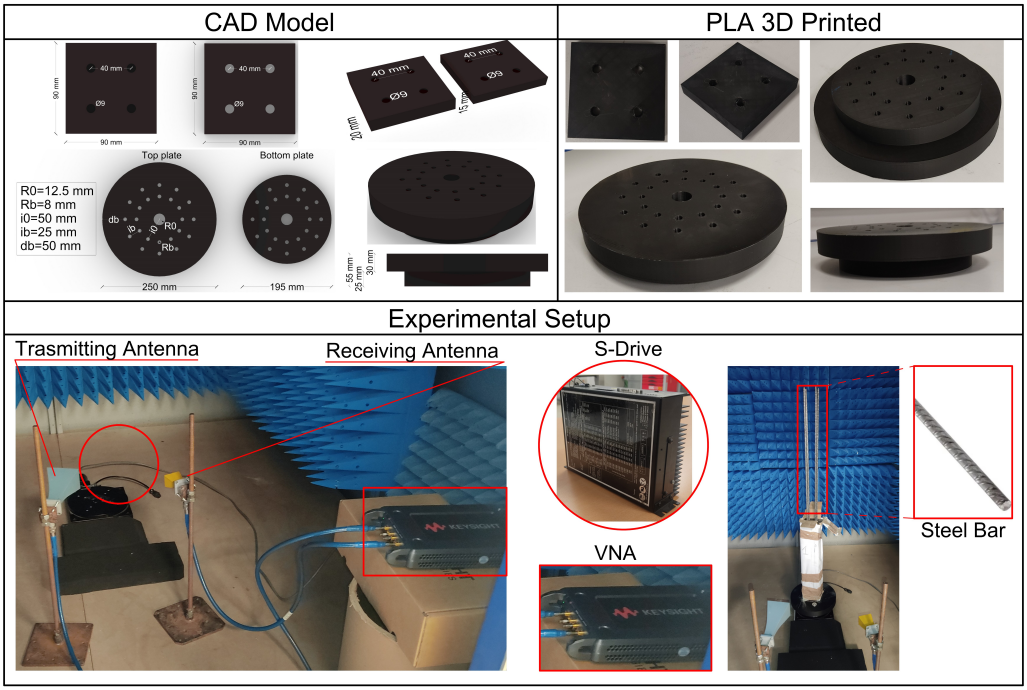

Figure 4. Experimental setup. On the left, the CAD model is shown, depicting the supports for the steel bars and the rotating basement. On the right, the supports printed in PLA material are shown. On the bottom, the instrumentation and one of the specimens employed for the experiment in the semi-anechoic environment are shown.

Firstly, standard Short–Open–Load–Through (SOLT) calibration of the Vector Network Analyzer (VNA) was performed for all the four scattering parameters (S_{ij}) at the end of the cables. This calibration is essential to prevent systematic errors in measurements arising from the non-uniformity of the components comprising the Network Analyzer, aiming to achieve its ideal performance with tolerances of ± 0.1 dB and $\pm 0.1°$. The measurement system is controlled via a laptop in the Matlab environment (MathWorks Inc., Natick, MA, USA). In particular, movement of the rotating table and VNA data acquisition are synchronized by means of an ad hoc script.

Measurement Results

Experimental tests were conducted on the previously described specimens, summarized for clarity in Table 1 and Figure 5.

Table 1. Number and type of specimens subjected to lab testing. Sand (S), Cement Powder (C), Sand and one Bar (S + 1B), Sand and three Bars (S + 3B), Sand and four Bars (S + 4B), Cement Powder and one Bar (C + 1B), Cement Powder and three Bars (C + 3B), Cement Powder and four Bars (C + 4B).

SPECIMENS 90 × 90 × 450 mm	
TEST	**TYPE**
1	S
2	C
3	S + 1B
4	S + 3B
5	S + 4B
6	C + 1B
7	C + 3B
8	C + 4B

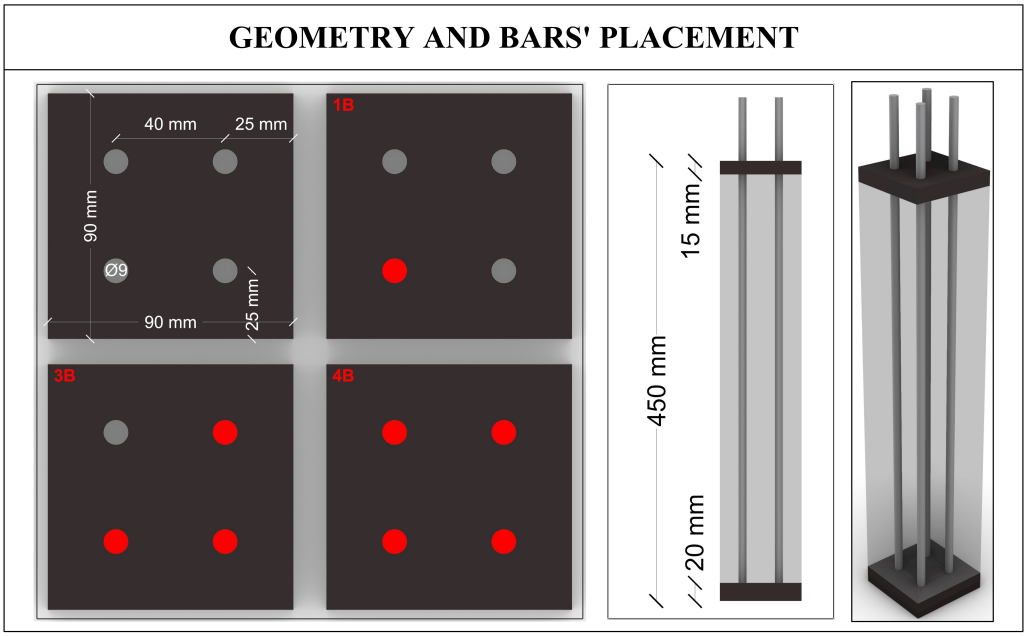

Figure 5. Geometry of specimens used in both experimental tests and numerical simulations.

For each measurement, all four scattering parameters S_{ij} with $i, j = 1, 2$ were acquired using the VNA for 1601 equispaced frequencies within the 8.2–12.4 GHz range. In the following, only the S_{21} parameter will be referenced, representing the transmission coefficient between the transmitter and receiver antennas (see Figure 4). The transmitting and receiving antennas are placed at the horizontal distances of $R_s = 42$ cm and $R_o = 49$ cm from the rotating table center, respectively, at the stand-off angle of $\theta_0 = 34^\circ$ (see Figure 3). At such distances, the specimen falls inside the main lobe of the radiation pattern of the antennas. Indeed, the width at 3 dB of the main lobe of our two horn antennas, calculated at 10 GHz, is around 30° for the most directive one and 60° for the other. Measurements of the specimens were conducted by performing a full rotation of the circular plate with an angular step of $\Delta\theta = 2^\circ$ (resulting in $N = 181$ angular positions for each measurement; the first and last positions coincide). This configuration is equivalent to moving the antennas over a circle around the target. Firstly, a measurement was taken without specimens to quantify the mutual coupling between the two antennas, which were kept in the same position as during the subsequent measurements of the specimens. Such a mutual coupling is subtracted from measurements in presence of different specimens. In Figure 6, the

moduli of the measurements obtained after subtraction of the mutual coupling are shown as a function of the angular position and frequency. It can be appreciated that the overall dynamic, contained below 0.03, is similar for both sand and cement powder targets with and without bars. Measurements without the bars appear very regular, with four angles where the modulus achieve its maxima. The peaks can be easily explained by resorting to geometric optics arguments: when the angular position is such that one of the four planar faces of the specimen is "seen" by the transmitting and receiving antennas under the same angle, the receiving antenna captures the reflected field. This circumstance occurs four times due to the complete rotation of the specimen.

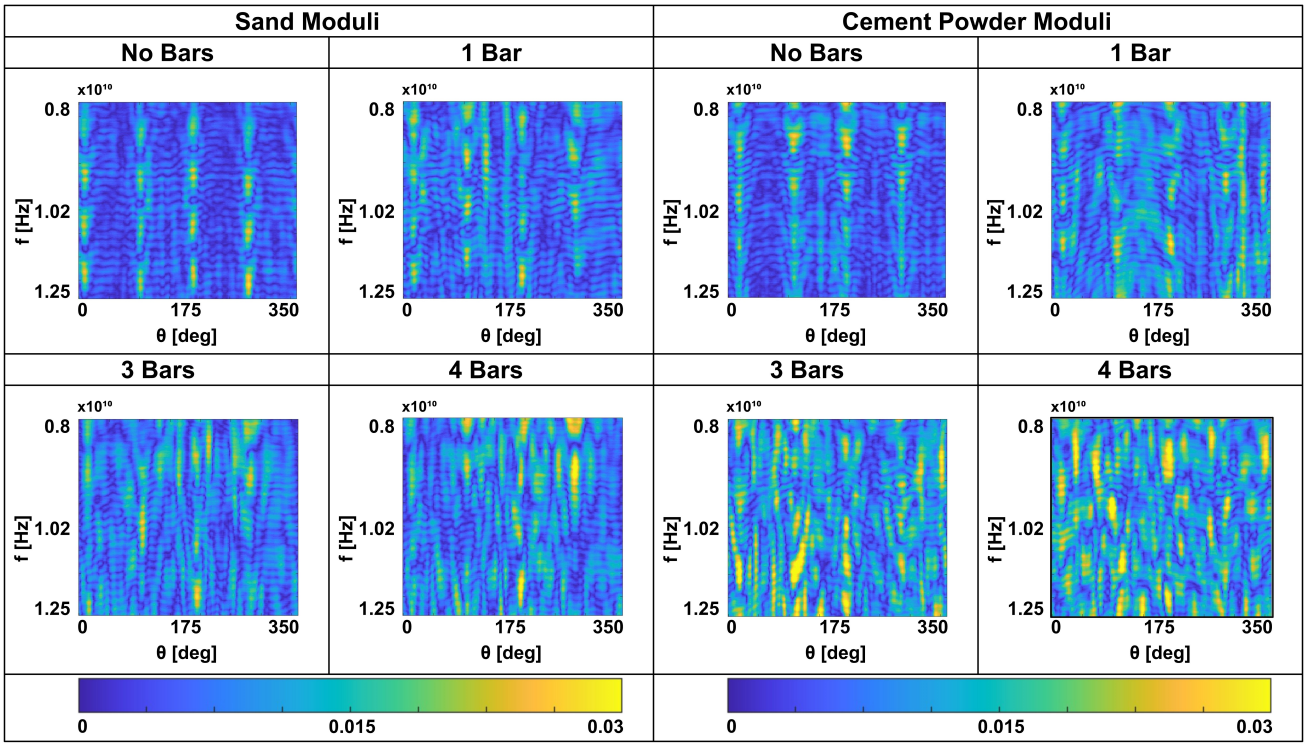

Figure 6. Experimental measurement of moduli of specimens with and without bars. Specimens filled with sand (**left**); specimens filled with cement powder (**right**).

Furthermore, the presence of bars inside the specimen causes further reflections that interact with those produced by the specimen faces either in a destructive or constructive way. The presence of one bar evidently "perturbs" the scattered field in the angular region, corresponding to the position at which the bar is closest to the antennas, whereas the presence of more bars perturbs the scattered field in almost all angular positions. In this sense, the presence of bars produces a "more chaotic" scattered field. This implies that the scattered field measured in the proposed configuration is able to determine information about the inside of the structure. It can be noted that the measurements of sand and of cement powder show slightly different amplitudes due to the different material permittivities. As a matter of fact, it is expected that the cement powder will have a higher dielectric permittivity than sand, as it is more compact because it has finer grains. In the laboratory, by means of the measurement of the "flight time" across the specimen, we roughly estimated the cement powder's relative permittivity to be $\varepsilon_r = 3$. In order to validate the experimental measurements, a comparison with simulated data is in order. The next section is dedicated to simulations of the field scattered by the cement powder specimens.

4. Numerical Simulations

Scattered field data were simulated using the open-source software GprMax (gprMax is currently released under the GNU General Public License v3) [28]. It is worth noting that this simulation software provides time-domain analyses. To obtain frequency-domain data, we utilized the available source waveform type *impulse* and post-processed the data following the procedure suggested in [29], which simulates a stepped-frequency radar.

We maintain the same geometry and target dimensions as in the experimental measurements: a square target with sides of $W = P = 9$ cm made from a dielectric material with a relative permittivity of $\varepsilon_r = 3$, representing cement powder, with one or more embedded bars. The presence of either one, three, or four bars is simulated using perfect electrically conducting cylinders with a diameter of 8 mm, positioned at the same locations as in the experimental tests (depicted in Figure 5).

The source is a *Hertzian dipole*, scanning a circle of radius $R_s = 42$ cm, while the observation point scans a circle of radius $R_o = 49$ cm at a stand-off angle of $\theta_0 = 34°$ with $N = 181$ steps of $\Delta\theta = 2°$. We employ the *impulse* waveform for the source, and the resulting A-scans are post-processed to obtain data at $N_f = 201$ equispaced frequencies in the X-band range of 8.2–12.4 GHz.

In Figures 7 and 8, we present the moduli and phases of the numerical scattered field data as functions of the frequency and angle. Although the numerical simulations exhibit a smoother pattern than the measurements, similar behavior is observed: maxima appear at four angles corresponding to the reflection positions when the dielectric does not contain embedded cylinders. The presence of bars, which interfere with the field propagating inside the dielectric, significantly alters the modulus and phase of the simulated scattered field. This evidence confirms the feasibility of detecting bars within cement using non-contact measurements in the X-band frequency range.

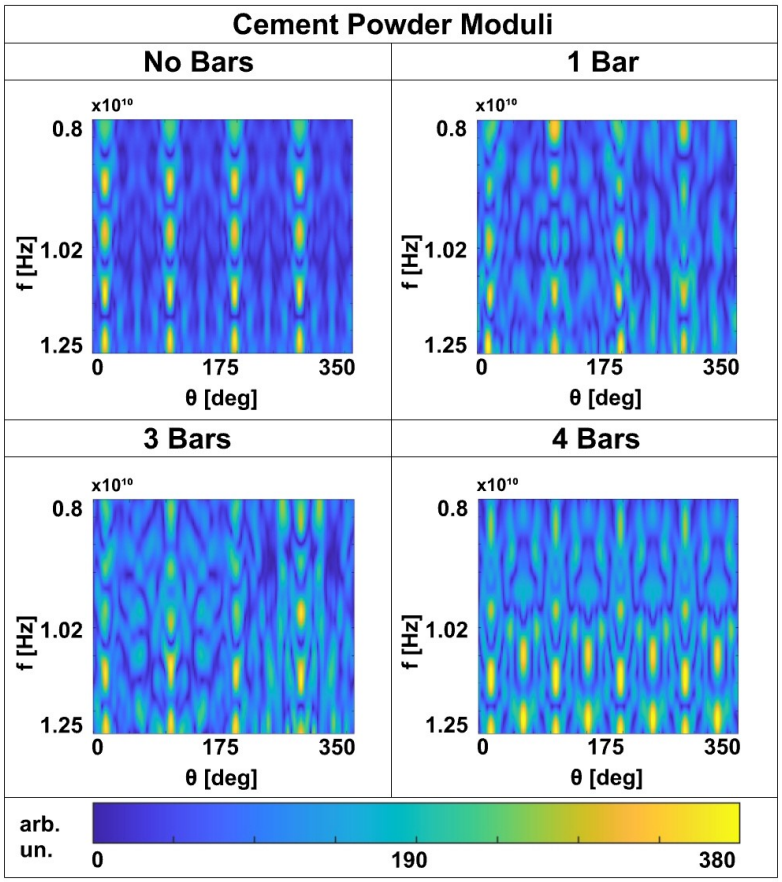

Figure 7. GprMax numerical simulations of the cement powder target. Scattered field moduli with and without bars.

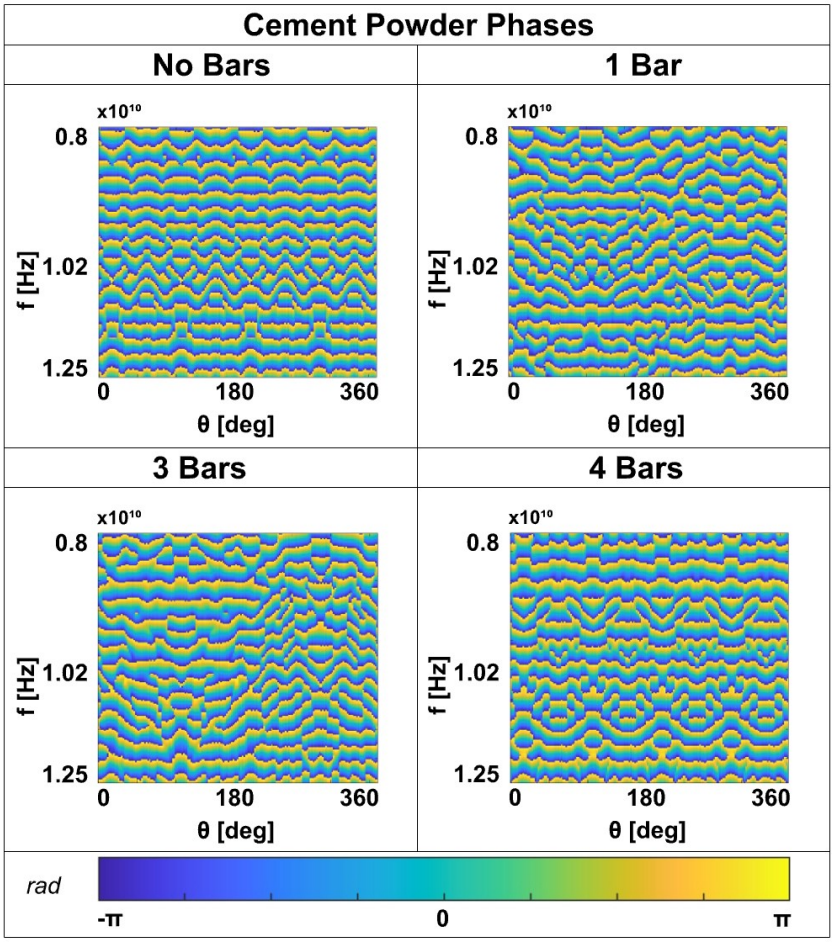

Figure 8. GprMax numerical simulations of the cement powder target. Scattered field phases with and without bars.

In order to further analyze the experimental measurements and to possibly introduce corrections useful for the subsequent detection stage, we compare simulation and experimental results in the time domain. This task is accomplished by performing the inverse fast Fourier transform (*ifft*) of the available frequency-domain data, thus obtaining a sort of radargram. Note that usually radargrams refer to antennas moving on a straight line, whereas in the case at hand, the spatial variable accounts for the angular displacement.

The radargram obtained by the numerical simulation without bars is used for calibration of the measurements. As a matter of fact, it allows us to appreciate the phase shift (due to the antenna's behavior) and the ripple (due to scattering from far surfaces present in the laboratory) which affect measurements, providing the way to correct such disturbances. For this scope, we preferred to use the radargram in the absence of bars because, as it is shown in Figure 6, bars introduce further reflections inside the cement, not useful for calibration purposes.

In Figure 9, the obtained *ifft* results for the GprMax simulated data and the measured data, in the case of cement powder without embedded bars, are shown and compared. It is worth noting two things. First, the experimental measurement appears delayed with respect to the simulation. This delay of approximately 1 ns can be better appreciated by looking at Figure 9 (top), where a cut of the radargrams is shown. The cut was made at two different angles because there is a slight shift between measurement and simulation, as can be seen in the same Figure 9 (bottom), showing the cut at the times of 3.85 ns and 2.85 ns, respectively.

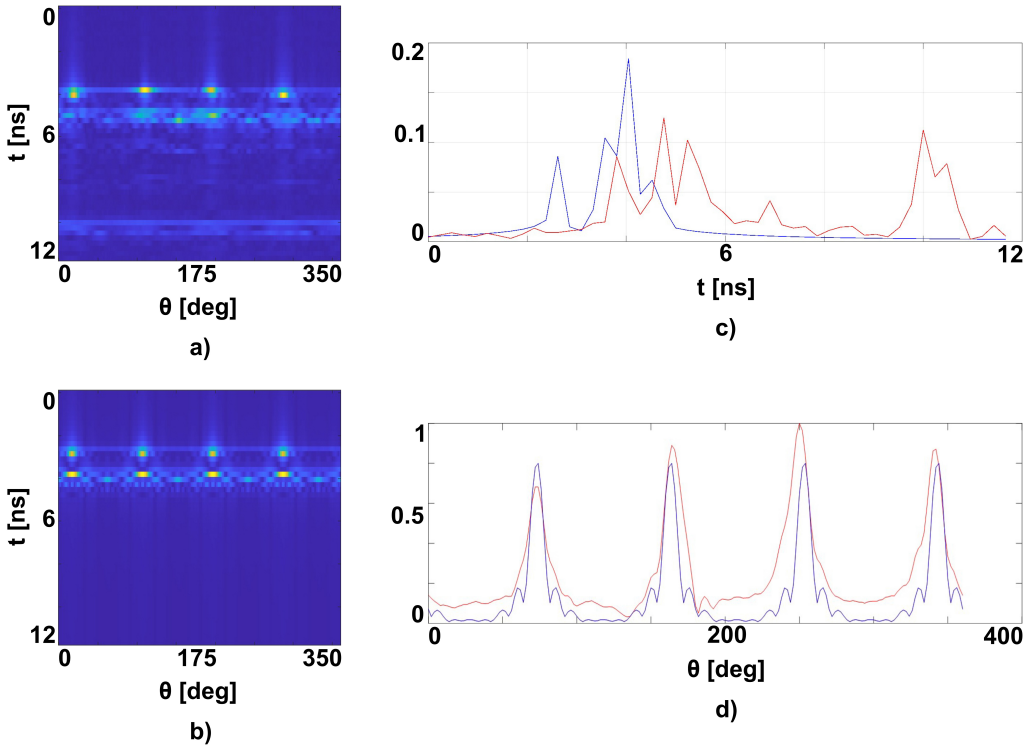

Figure 9. Comparison between experimental measurements (**a**) and GprMax simulations (**b**) in the time domain in cement powder without bars. On the right, the cut of the results shown in (**a**,**b**) are reported. (**c**) Time trace at 340° (measurement, red line) and 342° (simulation, blue line). (**d**) Angular trace at 3.85 ns (measurement, red line) and 2.85 ns (simulation, blue line).

Such a shift is due in particular to the limited precision of the measurement system alignment. The delay corresponds to a phase shift in the frequency-domain data due to a path difference of 30 cm (in air), which is perfectly compatible with the fact that the standard calibration of the VNA is performed up to the input of the antennas and therefore does not consider the path between the connector and the radiating aperture. The measured data reported in Figure 9a also show a reflection between 9 ns and 10 ns due to the non-perfect anechoic environment. Such a reflection is responsible for the ripple that is observed in the measurements moduli in Figure 6. A comparison with simulated data suggests correcting the measurements by adding a linear phase and filtering out reflections coming from objects far from the investigated specimen.

5. Bar Detection

The numerical simulated data reported in the previous section were processed by using the above summarized algorithm, introduced in [26]. In particular, Equation (5) is discretized by using $N = 181$ equispaced angles $\theta = n\Delta\theta, n = 0, ..., N$, with $\Delta\theta = 2^\circ$ and $N_f = 201$ equispaced frequencies inside the X-band (8.2–12.4 GHz), thus providing $N \times N_f$ equations and N_b unknowns. Inversion was performed by means of TSVD of the obtained matrix. Simulated data were corrupted by adding Gaussian noise so that $SNR = 6$, and the singular value truncation index was chosen accordingly. Finally, a threshold equal to 0.55 was applied to the normalized modulus of the estimated function $\gamma(n)$. The bars occupy one, three or four of these "candidate" positions. It is not known a priori how many bars there are. The indexes where the estimated function is equal to one indicate that a bar is present in those positions. The inversion results obtained by processing GprMax simulated data are shown in Figure 10 and confirm the feasibility of detecting and localizing embedded bars using high-frequency contactless data.

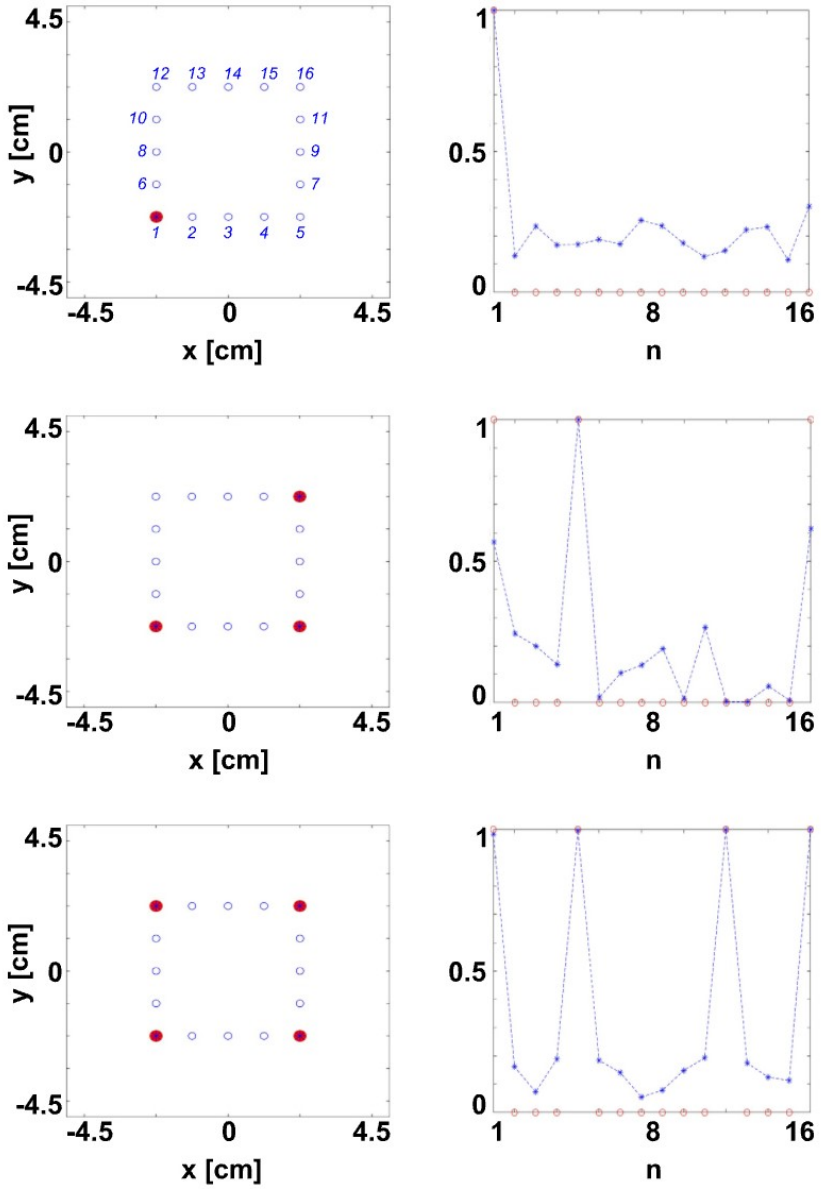

Figure 10. Detection and localization by GprMax simulated scattered field data. The bars are numbered progressively from left to right and from bottom to top. On the left, candidate (blue circles), actual (red circles) and estimated (blue stars) positions are shown. On the right, the estimated $|\gamma(n)|$ is plotted versus the position index.

6. Conclusions

The preliminary experimental results presented in this work highlight the field's ability to penetrate cement, revealing crucial insights into embedded bars through scattered data. By applying a quasi-quadratic inverse scattering technique to numerically simulated data, promising results have been achieved, confirming the reliability of the proposed approach. This success is further supported by a qualitative comparison between experimental and numerical results, reinforcing the consistency of our approach.

Notably, using a higher frequency enables the use of lighter equipment and smaller antennas, representing a step forward in advancing non-destructive testing (NDT) methods for detecting and localizing steel bars within concrete structures.

However, several areas for refinement and improvement have been identified. Firstly, it is crucial to account for the angular and frequency behavior of antennas in the mathematical model to ensure a good measurement accuracy. Moreover, establishing the precise external morphology and spatial orientation of the target section relative to the antennas is

essential, particularly considering potential material-induced deformations. Nevertheless, we anticipate that transitioning from powder-based specimens to solid, reinforced concrete structures will mitigate some of these challenges encountered in laboratory settings. Additionally, accurately determining concrete's relative permittivity and conductivity is essential for optimizing the present procedure, although this falls beyond the scope of this study. Preliminary measurements of permittivity values have been experimentally retrieved; a comprehensive knowledge of these properties remains crucial. Finally, by overcoming these challenges, the proposed strategy could pave the way for enhancing non-invasive testing, further improving structural health monitoring and preventing unforeseen disasters.

Author Contributions: Conceptualization, A.B.; methodology, A.B. and S.P.; software, A.B. and S.P.; validation, A.B. and S.P.; formal analysis, A.B.; investigation, A.B. and S.P.; resources, A.B. and S.P.; data curation, A.B. and S.P.; writing—original draft preparation, A.B. and S.P.; writing—review and editing, A.B. and S.P.; visualization, S.P.; supervision, A.B.; project administration, A.B. and S.P.; funding acquisition, A.B. All authors have read and agreed to the published version of the manuscript.

Funding: This work was supported by the European Union NextGenerationEU, call PRIN 2022, project ARACNE—A RAdar system for Contactless surveys of reiNforced concrEte (grant n. 202225CSP2).

Data Availability Statement: The data presented in this study are available in this article.

Conflicts of Interest: The authors declare no conflicts of interest.

References

1. Bensaber, A.; Boudaoud, Z.; Seghir, N.; Czarnecki, S.; Sadowski, L. The assessment of concrete subjected to compressive and flexural preloading using nondestructive testing methods, correlation between concrete strength and combined method (SonReb). *Meas. J. Int. Meas. Confed.* **2023**, *222*, 113659. [CrossRef]
2. Yin, T.; Ng, C.; Chen, L.; Kotousov, A. In-situ nonlinear ultrasonic technique for monitoring damage in ultra-high performance fibre reinforced concrete (UHPFRC) during direct tensile test. *Meas. J. Int. Meas. Confed.* **2023**, *222*, 113587. [CrossRef]
3. Kuchipudi, S.; Ghosh, D. Automated detection and segmentation of internal defects in reinforced concrete using deep learning on ultrasonic images. *Constr. Build. Mater.* **2024**, *411*, 134491. [CrossRef]
4. Alavi, S.; Noel, M.; Moradi, F.; Layssi, H. Development of a machine learning model for on-site evaluation of concrete compressive strength by SonReb. *J. Build. Eng.* **2024**, *82*, 108328. [CrossRef]
5. Jena, B.; Zade, N.P.; Sarkar, P.; Karak, S.K. Sustainable integration of coal mine overburden as a substitute for natural sand in concrete to enhance its mechanical and durability properties. *Constr. Build. Mater.* **2024**, *411*, 134488. [CrossRef]
6. Parhi, S.K.; Patro, S.K. Application of R-curve, ANCOVA, and RSM techniques on fracture toughness enhancement in PET fiber-reinforced concrete. *Constr. Build. Mater.* **2024**, *411*, 134644. [CrossRef]
7. Keo, S.A.; Szymanik, B.; Roy, C.L.; Brachelet, F.; Defer, D. Defect Detection in CFRP Concrete Reinforcement Using the Microwave Infrared Thermography (MIRT) Method—A Numerical Modeling and Experimental Approach. *Appl. Sci.* **2023**, *13*, 8393. [CrossRef]
8. Woldeamanuel, M.M.; Kim, T.; Cho, S.; Kim, H.K. Estimation of concrete strength using thermography integrated with deep-learning-based image segmentation: Case studies and economic analysis. *Expert Syst. Appl.* **2023**, *213*, 119249. [CrossRef]
9. Cheng, Z.; Zhao, H.; Long, G.; Yang, K.; Chen, M.; Wu, Z. The Mechanical Characteristics of High-Strength Self-Compacting Concrete with Toughening Materials Based on Digital Image Correlation Technology. *Materials* **2023**, *16*, 1695. [CrossRef] [PubMed]
10. Herbers, M.; Richter, B.; Gebauer, D.; Classen, M.; Marx, S. Crack monitoring on concrete structures: Comparison of various distributed fiber optic sensors with digital image correlation method. *Struct. Concr.* **2023**, *24*, 6123–6140. [CrossRef]
11. Xu, X.; Jin, Z.; Yu, Y.; Li, N. Damage source and its evolution of ultra-high performance concrete monitoring by digital image correlation and acoustic emission technologies. *J. Build. Eng.* **2023**, *65*, 105734. [CrossRef]
12. Palladino, S.; Minutolo, V.; Esposito, L. Hybrid semi-analytical calculation of the stress intensity factor for heterogeneous and functionally graded plates. *Eng. Fract. Mech.* **2022**, *274*, 108763. [CrossRef]
13. Esposito, L.; Palladino, S.; Minutolo, V. An effective free-meshing and linear Step-Wise procedure to predict crack initiation and propagation. *Theor. Appl. Fract. Mech.* **2024**, *130*, 104240. [CrossRef]
14. Zona, R.; Minutolo, V. A dislocation-based finite element method for plastic collapse assessment in solid mechanics. *Arch. Appl. Mech.* **2024**, *94*, 1531–1552. [CrossRef]
15. Sagar, R.V.; Basu, D.J. Damage assessment of reinforced concrete structures under elevated-amplitude cyclic loading using sentry values based on acoustic emission testing. *Nondestruct. Test. Eval.* **2023**, *38*, 612–630. [CrossRef]
16. Ma, G.; Xie, Y.; Long, G.; Tang, Z.; Tang, C.; Wang, H.; Wei, Y.; Li, J. Experimental study on acoustic emission and surface morphology characteristics of concrete under different fracture modes. *Theor. Appl. Fract. Mech.* **2023**, *123*, 103702. [CrossRef]

17. Robert, A. Dielectric permittivity of concrete between 50 MHz and 1 GHz and GPR measurements for building materials evaluation. *J. Appl. Geophys.* **1998**, *40*, 89–94. [CrossRef]
18. Barrile, V.; Pucinotti, R. Application of radar technology to reinforced concrete structures: A case study. *NDT E Int.* **2005**, *38*, 596–604. [CrossRef]
19. Pasculli, D.; Natali, A.; Salvatore, W.; Morelli, F.; Morandi, D. Investigation of reinforced concrete bridges by using a dual-polarized high-frequency GPR. In Proceedings of the 2018 17th International Conference on Ground Penetrating Radar, GPR 2018, Rapperswil, Switzerland, 18–21 June 2018. [CrossRef]
20. Rhee, J.Y.; Choi, J.J.; Kee, S.H. Evaluation of the Depth of Deteriorations in Concrete Bridge Decks with Asphalt Overlays Using Air-Coupled GPR: A Case Study from a Pilot Bridge on Korean Expressway. *Int. J. Concr. Struct. Mater.* **2019**, *13*, 23. [CrossRef]
21. Tosti, F.; Ferrante, C. 3 Using Ground Penetrating Radar Methods to Investigate Reinforced Concrete Structures. *Surv. Geophys.* **2020**, *41*, 485–530. [CrossRef]
22. Dinh, K.; Gucunski, N.; Duong, T.H. Migration-based automated rebar picking for condition assessment of concrete bridge decks with ground penetrating radar. *NDT E Int.* **2018**, *98*, 45–54. [CrossRef]
23. Marchisotti, D.; Zappa, E. Feasibility Study of Drone-Based 3-D Measurement of Defects in Concrete Structures. *IEEE Trans. Instrum. Meas.* **2022**, *71*, 5010711. [CrossRef]
24. Catapano, I.; Gennarelli, G.; Ludeno, G.; Noviello, C.; Esposito, G.; Soldovieri, F. Contactless ground penetrating radar imaging: State of the art, challenges, and microwave tomography-based data processing. *IEEE Geosci. Remote. Sens. Mag.* **2021**, *10*, 251–273. [CrossRef]
25. Boldrin, P.; Fornasari, G.; Rizzo, E. Review of Ground Penetrating Radar Applications for Bridge Infrastructures. *NDT* **2024**, *2*, 53–75. [CrossRef]
26. Brancaccio, A. A Quasi-Quadratic Inverse Scattering Approach to Detect and Localize Metallic Bars within a Dielectric. *Appl. Sci.* **2022**, *12*, 9217. [CrossRef]
27. Daniels, D.J. *Ground Penetrating Radar*; The Institution of Electrical Engineers: London, UK, 2004; Volume 1. [CrossRef]
28. Warren, C.; Giannopoulos, A.; Giannakis, G. gprMax: Open source software to simulate electromagnetic wave propagation for Ground Penetrating Radar. *Comput. Phys. Commun.* **2016**, *209*, 163–170. [CrossRef]
29. Day 3—Impulse Response & Introduction to SFCW GPR Simulation—Dr Antonis Giannopoulos. Available online: https://www.youtube.com/watch?v=_FWNeqTr9nc (accessed on 5 March 2024).